Lattice dynamics of fluoride scheelites: II. Inelastic neutron scattering in $LiYF_4$ and modelization

1997 J. Phys.: Condens. Matter 9 6957

(http://iopscience.iop.org/0953-8984/9/32/017)

J. Phys.: Condens. Matter **9** (1997) 6957–6968. Printed in the UK PII: S0953-8984(97)80395-5

Lattice dynamics of fluoride scheelites: II. Inelastic neutron scattering in $LiYF_4$ and modelization

S Salaün†, A Bulou†, M Rousseau†, B Hennion‡ and J Y Gesland†

† Laboratoire de Physique de l'Etat Condensé, Faculté des Sciences, Université du Maine, Avenue O Messiaen, 72017 Le Mans Cedex, France

‡ Laboratoire Léon Brillouin, CEA-CENS Saclay, 92290 Gif-sur-Yvette Cedex, France

Received 18 December 1996

Abstract. A general view of the fluoride scheelite $LiYF_4$ lattice dynamical properties is proposed. The symmetry properties of the vibrations and the symmetry-adapted eigenvectors of the scheelite structure have been determined for the most important directions of the Brillouin zone, namely $(\xi 00)$, $(\xi\xi 0)$ and (00ξ). The low-frequency phonon spectrum along these three directions has been measured by inelastic neutron scattering. The corresponding data, together with the measured sound velocities and the Raman- and infrared-active phonon frequencies, are described in the framework of a rigid ion model. The average error between experimental results and calculated frequencies is less than 5%. The most important normal modes of vibration and the one-phonon density of states are deduced.

1. Introduction

Compounds which crystallize in the scheelite structure are the subject of many studies, mainly because generally they are optically transparent insulators and are of interest in laser optical studies [1]. Among these compounds, as already mentioned in paper I, $LiYF_4$ is the most widely used fluoride laser host crystal, generally doped with trivalent rare-earth ions ($Nd^{3+}, Eu^{3+}, \ldots$) and, more recently, with uranium [2]. On the other hand, some oxide scheelites, namely $BiVO_4$ and $LaNbO_4$, undergo a pseudo proper ferroelastic phase transition, which is a quite rare phenomenon [3]. The luminescence-line profiles (provided that the electron–phonon coupling is not negligible) and the mechanism of the phase transition depend on the phonon spectra of the corresponding material, but none of the scheelite phonon dispersion curves or density of states have ever been published.

The purpose of the present paper is to provide bases for the description of the lattice dynamics of scheelites, supported by the results of an experimental study on $LiYF_4$. This fluoride scheelite has been chosen with regard to its technological importance and to the large number of experimental data already available in the literature (elastic constants, Raman and infrared frequencies). Moreover, large $LiYF_4$ single crystals are produced for laser applications, which enables inelastic neutron scattering measurements of the low-frequency phonon spectrum in good conditions. The choice of a fluoride scheelite like $LiYF_4$ is also dictated by the weak ions polarizabilities: this is a prerequisite for the use of a simple description of the phonon spectrum, like a rigid ion model, involving a small number of parameters. Actually, most of the force constants can be estimated from the data available in the literature [4], what reduces the number of adjustable parameters and ensures to obtain the most simple and tractable information about lattice dynamics in this structure. The

0953-8984/97/326957+12$19.50

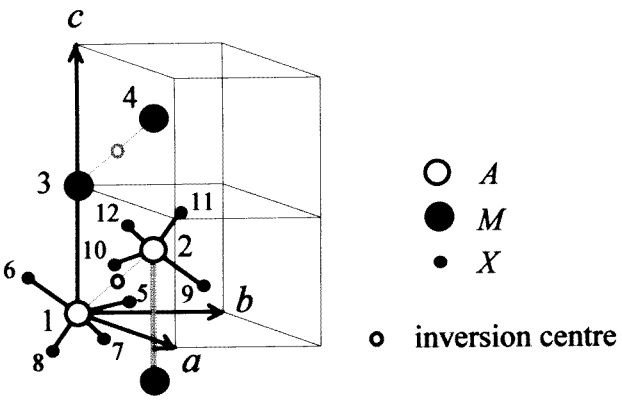

Figure 1. The unit of structure of scheelite compounds AMX_4, represented in the tetragonal crystallographic basis $(\boldsymbol{a}, \boldsymbol{b}, \boldsymbol{c})$. The symmetry centre, which relates the two formula units, lies at $(0, \frac{1}{4}, \frac{1}{8})$. The labelling of the atoms, already used in paper I, is developed in table 2.

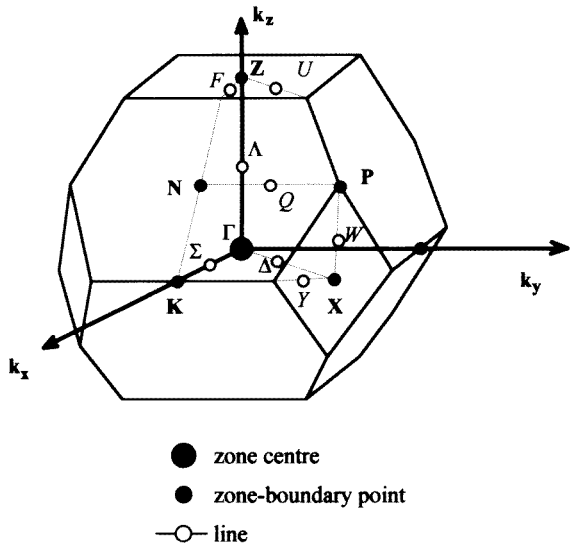

Figure 2. The Brillouin zone of a tetragonal body-centred structure with $c > a$.

calculation and refinement of the phonon spectrum by a rigid ion model also allows us to report in this paper the main atomic movements under some of the zone-centre vibrational modes, and the one-phonon density of states.

The group theory analysis of the scheelite structure vibrations is reported in section 2, the experimental determination of the low-frequency modes of $LiYF_4$ by inelastic neutron scattering will be described in section 3 and the modelization by a rigid ion model will be introduced and compared with experiment reults in section 4.

Table 1. Distribution of the scheelites vibrational modes for points of the Brillouin zone among the irreducible representations (IR) of the wavevector's point group $G_0(\boldsymbol{q})$ (sub-group of C_{4h}, indicated in parentheses). The compatibility relations between the symmetry types of the lattice vibrations are symbolized by continuous lines. Note that all the modes at the Z and X points are doubly degenerated.

$\Gamma(C_{4h})$ $\boldsymbol{q}=(0,0,0)$	$\Sigma(C_h)$ $\boldsymbol{q}=(q,0,0)$ $(q<q(K))$	$F(C_h)$ $\boldsymbol{q}=(q,0,0)$ $(q>q(K))$	$Z(C_{4h})$ $\boldsymbol{q}\left(0,0,\frac{2\pi}{c}\right)$	$\Lambda(C_4)$ $\boldsymbol{q}=(0,0,q)$	Γ	$\Delta(C_h)$ $\boldsymbol{q}=\frac{1}{\sqrt{2}}(q,q,0)$	$X(C_{2h})$ $\boldsymbol{q}=\left(\frac{\pi}{a},\frac{\pi}{a},0\right)$

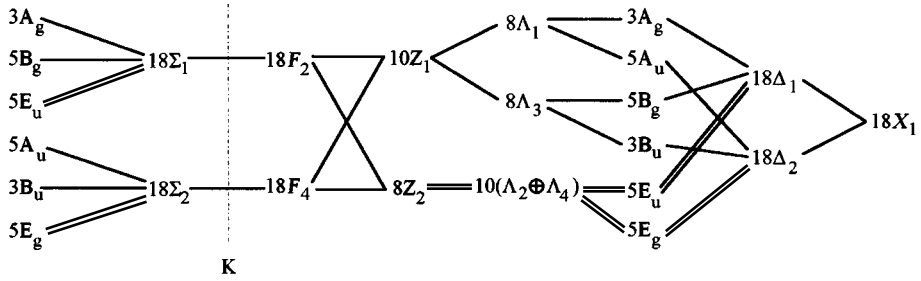

2. Symmetry types of the lattice modes

Scheelite compounds belong to the $I4_1/a(C_{4h}^6)$ space group and their body-centred tetragonal cell, shown in paper I, contains four formula units, i.e. two AMX_4 units per primitive cell (figure 1); hence there are 36 vibrational modes for each $\boldsymbol{q}$ vector in the reciprocal space.

The symmetry analysis of the vibrational modes has been performed for the most representative reciprocal directions in this structure, namely the so-called ΓKZ, ΓZ and ΓX lines (figure 2). For the corresponding $\boldsymbol{q}$ vectors, the distribution of the 36 vibration modes among the irreducible representations of the wavevector group $G_0(\boldsymbol{q})$ is done following the method of Maradudin and Vosko [5]. The results are listed in table 1 together with the compatibility relations, the irreducible representations being labelled according to a choice of origin at the Li site. We used the notation of Zak *et al* [6] for inner and boundary points of the Brillouin zone, and the more usual notation of Wigner and Mulliken for zone-centre phonons.

The corresponding symmetry-adapted displacement vectors are given in table 2 for inner and boundary high-symmetry points. Results for the zone centre are reported in paper I.

As shown in table 1, the number of different irreducible representations is rather small out of the zone centre: only one possible symmetry at the X point, two different symmetries for Z point, ΓKZ and ΓX lines, and finally three on the ΓZ line, one being doubly degenerated.

3. Measurements of the low-frequency phonon spectrum

3.1. Experimental details

The single crystal of $LiYF_4$ used for the experiments has been grown by J Y Gesland, using the Czochralski technique, the pull-out axis being a. The crystallographic parameters are $a = b = 5.279$ Å and $c = 11.021$ Å [7].

The inelastic neutron-scattering measurements have been performed at the Laboratory Léon Brillouin ('LLB', Saclay, France), at room temperature on the thermal-beam triple-axis spectrometer 1T. A final wavevector of the neutron $k_f = 2.662$ Å^{-1} has been used,

Table 2. Symmetry-adapted vectors in the scheelite structure determined by a group theory analysis for the main points and lines of the Brillouin zone. The ρ_j coefficients are defined as $e^{i\pi\alpha_j}$, α_j being the jth reduced coordinate of the $\boldsymbol{q}$-vector in the basis $(\boldsymbol{a}^*, \boldsymbol{b}^*, \boldsymbol{c}^*)$ ($\rho = \rho_3$ for the ΓZ line). a_i, b_i and c_i coefficients may be complex. The modes with Z_1, Z_2, $\Lambda_{2\oplus4}$ or X_1 symmetries are doubly degenerated: the second eigenvector may be deduced from the first by complex conjugation.

Atom (no.) (reduced coordinates)	$\Gamma K Z(\xi,0,0)$		$\Gamma Z(0,0,\xi)$			$\Gamma X(\xi,\xi,0)$		$X(\frac{1}{2},\frac{1}{2},0)$	$Z(0,0,1)$	
	Σ_1	Σ_2								
	F_2	F_4	$\Lambda_{2\oplus4}$	Λ_1	Λ_3	Δ_1	Δ_2	X_1	Z_1	Z_2
Li(1)	a_1	a_1	a_1	0	0	a_1	a_1	a_1	0	a_1
(0, 0, 0)	b_1	b_1	b_1	0	0	b_1	b_1	b_1	0	b_1
	c_1	c_1	0	c_1	c_1	c_1	c_1	c_1	c_1	0
Li(2)	a_1	$-a_1$	a_2	0	0	$\rho_2 a_1$	$-\rho_2 a_1$	ia_1	0	a_2
$(0, \frac{1}{2}, \frac{1}{4})$	b_1	$-b_1$	b_2	0	0	$\rho_2 b_1$	$-\rho_2 b_1$	ib_1	0	b_2
	$-c_1$	c_1	0	ρc_1	$-\rho c_1$	$-\rho_2 c_1$	$\rho_2 c_1$	$-ic_1$	ic_1	0
Y(3)	a_2	a_2	a_3	0	0	a_2	a_2	a_2	0	a_3
$(0, 0, \frac{1}{2})$	b_2	b_2	b_3	0	0	b_2	b_2	b_2	0	b_3
	c_2	c_2	0	c_2	c_2	c_2	c_2	c_2	ic_2	0
Y(4)	a_2	$-a_2$	a_4	0	0	$\rho_2 a_2$	$-\rho_2 a_2$	ia_2	0	a_4
$(0, \frac{1}{2}, \frac{3}{4})$	b_2	$-b_2$	b_4	0	0	$\rho_2 b_2$	$-\rho_2 b_2$	ib_2	0	b_4
	$-c_2$	c_2	0	$-\rho c_2$	$-\rho c_2$	$-\rho_2 c_2$	$\rho_2 c_2$	$-ic_2$	c_2	0
F(5)	a_3	a_3	a_5	a_3	a_3	a_3	a_3	a_3	a_3	a_5
(x, y, z)	b_3	b_3	b_5	b_3	b_3	b_3	b_3	b_3	b_3	b_5
	c_3	c_3	c_5	c_3	c_3	c_3	c_3	c_3	c_3	c_5
F(6)	a_4	a_4	a_5	$-a_3$	$-a_3$	a_4	a_4	a_4	$-a_3$	a_5
$(-x, -y, z)$	b_4	b_4	b_5	$-b_3$	$-b_3$	b_4	b_4	b_4	$-b_3$	b_5
	c_4	c_4	$-c_5$	c_3	c_3	c_4	c_4	c_4	c_3	$-c_5$
F(7)	a_5	a_5	a_6	a_4	a_4	a_5	a_5	a_5	a_4	a_6
$(-y, x, -z)$	b_5	b_5	b_6	b_4	b_4	b_5	b_5	b_5	b_4	b_6
	c_5	c_5	c_6	c_4	c_4	c_5	c_5	c_5	c_4	c_6
F(8)	a_6	a_6	a_6	$-a_4$	$-a_4$	a_6	a_6	a_6	$-a_4$	a_6
$(y, -x, -z)$	b_6	b_6	b_6	$-b_4$	$-b_4$	b_6	b_6	b_6	$-b_4$	b_6
	c_6	c_6	$-c_6$	c_4	c_4	c_6	c_6	c_6	c_4	$-c_6$
F(9)	a_3	$-a_3$	a_7	ρb_4	$-\rho b_4$	$\rho_2 a_3$	$-\rho_2 a_3$	ia_3	ib_4	a_7
$(x, y+\frac{1}{2}, \frac{1}{4}-z)$	b_3	$-b_3$	b_7	$-\rho a_4$	ρa_4	$\rho_2 b_3$	$-\rho_2 b_3$	ib_3	$-ia_4$	b_7
	$-c_3$	c_3	c_7	ρc_4	$-\rho c_4$	$-\rho_2 c_3$	$\rho_2 c_3$	$-ic_3$	ic_4	c_7
F(10)	a_4	$-a_4$	a_7	$-\rho b_4$	ρb_4	$\rho_2 a_4$	$-\rho_2 a_4$	ia_4	$-ib_4$	a_7
$(-x, \frac{1}{2}-y, \frac{1}{4}-z)$	b_4	$-b_4$	b_7	ρa_4	$-\rho a_4$	$\rho_2 b_4$	$-\rho_2 b_4$	ib_4	ia_4	b_7
	$-c_4$	c_4	$-c_7$	ρc_4	$-\rho c_4$	$-\rho_2 c_4$	$\rho_2 c_4$	$-ic_4$	ic_4	$-c_7$
F(11)	a_5	$-a_5$	a_8	$-\rho b_3$	ρb_3	$\rho_2 a_5$	$-\rho_2 a_5$	ia_5	$-ib_3$	a_8
$(-y, x+\frac{1}{2}, \frac{1}{4}+z)$	b_5	$-b_5$	b_8	ρa_3	$-\rho a_3$	$\rho_2 b_5$	$-\rho_2 b_5$	ib_5	ia_3	b_8
	$-c_5$	c_5	c_8	ρc_3	$-\rho c_3$	$-\rho_2 c_5$	$\rho_2 c_5$	$-ic_5$	ic_3	c_8
F(12)	a_6	$-a_6$	a_8	ρb_3	$-\rho b_3$	$\rho_2 a_6$	$-\rho_2 a_6$	ia_6	ib_3	a_8
$(y, \frac{1}{2}-x, \frac{1}{4}+z)$	b_6	$-b_6$	b_8	$-\rho a_3$	ρa_3	$\rho_2 b_6$	$-\rho_2 b_6$	ib_6	$-ia_3$	b_8
	$-c_6$	c_6	$-c_8$	ρc_3	$-\rho c_3$	$-\rho_2 c_6$	$\rho_2 c_6$	$-ic_6$	ic_3	$-c_8$

with a pyrolytic graphite filter preventing high-order contamination.

Because of symmetry considerations, experimental data had to be collected in three different scattering planes, namely $(hk0)$, $(h0l)$ and (hhl). Because of the large neutron absorption cross section of natural lithium, we used different slabs for the measurements:

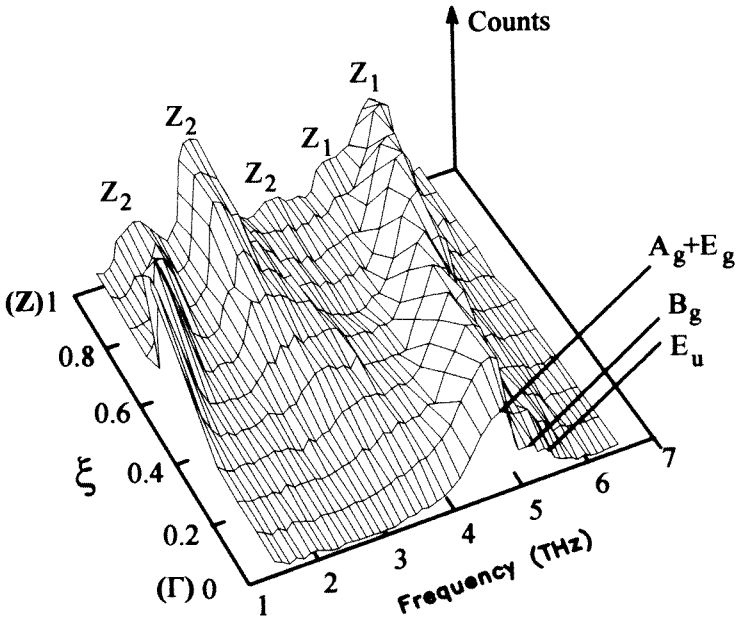

Figure 3. The inelastic neutron-scattering experimental spectra obtained at room temperature with a constant transfer vector $\boldsymbol{Q} = (4, 0, \xi)$, ξ varying from 0 (Γ point) to 1 (Z point), in the frequency range [1, 6 THz]. The symmetry of the zone-centre and zone-boundary modes has been indicated.

one cut perpendicularly to the four-fold axis c ($21 \times 20 \times 5$ mm^3) for the ($h0l$) and (hhl) scattering planes, and another cut perpendicularly to the a-axis ($31 \times 26 \times 5$ mm^3) for the ($hk0$) and ($h0l$) planes.

Due to the complexity of the phonon spectrum, we had to proceed in a self-consistent way, with the help of dynamical structure factor calculations based on a rigid ion model (see section 4) adjusted with the acquired experimental results.

3.2. Data analysis and results

The experimental data were treated with the help of a fitting program ($AFIT$ of the LLB) in order to obtain parameters as physically meaningful as possible. The program takes into account the resolution function of the spectrometer and calculates the lineshape by folding this resolution function with the neutron scattering cross section where the phonon modes are taken as damped harmonic oscillators. The dispersion of the modes is accounted for in a linear approximation. The energy, width and intensity of the oscillators are then deduced by fitting the calculated lineshapes to the experimental data. In many cases, due to the complexity of the phonon spectrum, we had to use self-consistently the dynamical structure factor calculations to fix the number of modes involved in a given measurement. Figure 3 illustrates this difficulty: the intensity measured in $(\boldsymbol{Q}, \omega)$ space, along the ΓZ line $(4, 0, \xi)$ with $\xi = 0$–1, is displayed, revealing the rapid evolution with ξ of the intensity of the vibrational modes.

The phonon frequencies for wavevectors in the three main symmetry directions [100], [110] and [001] have been reported in figure 4 together with the calculated dispersion curves obtained from the model which will be presented in detail below.

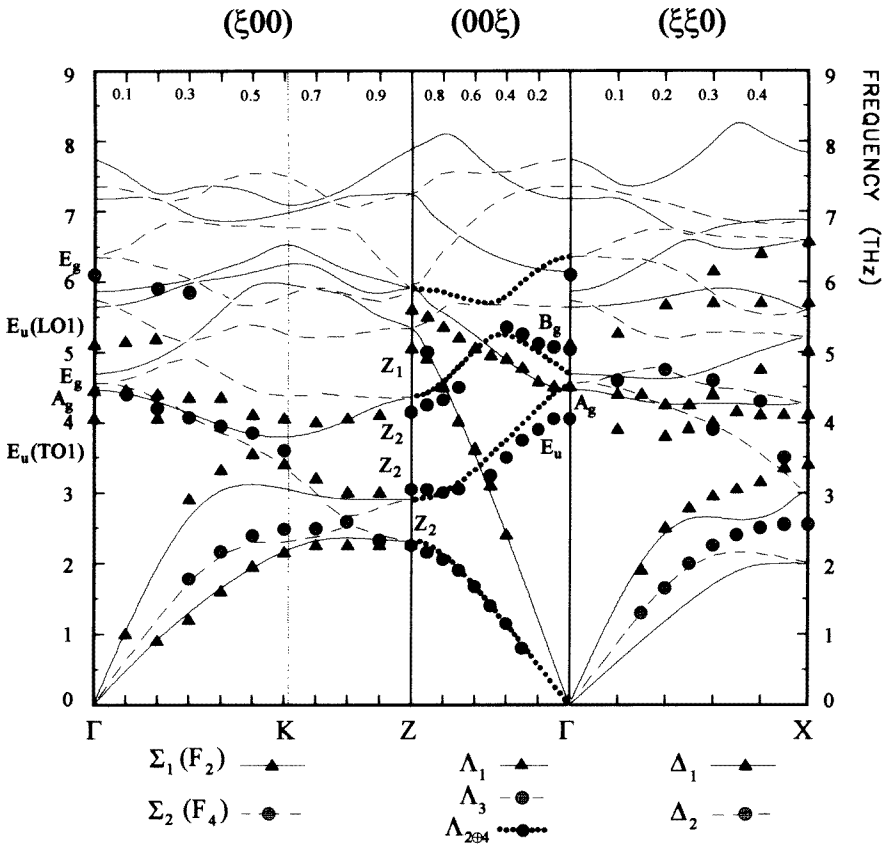

Figure 4. Experimental phonon frequencies measured by inelastic neutron scattering in $LiYF_4$ at room temperature together with the calculated phonon dispersion curves on the ΓKZ, $Z\Gamma$ and ΓX lines of the Brillouin zone (limited on the graph to 8 THz for clarity).

4. Calculation of the phonon spectrum

The phonon spectrum of $LiYF_4$ has been calculated with a rigid ion model (RIM) [8]. It is quite clear that such a model is not ideal to account for the experimental observations. But our main purpose is to deal with as few adjustable parameters as possible, including those which can be estimated from data reported in the literature [4], in order to get a description of the lattice dynamics which could be used for other scheelites. This choice is nevertheless expected to be reasonable as $LiYF_4$ has only weak ionic polarizability.

4.1. Parameters of the rigid ion model

Following Cowley [9], the short-range potential energy is considered as a sum of axially symmetric pair interactions. Two force constants correspond to each pair given by the second derivative of the corresponding short-range potential V_i, namely:

$$A_i = \frac{\partial^2 V_i}{\partial r_{i//}^2}\Big)_{\text{eq}} \qquad B_i = \frac{\partial^2 V_i}{\partial r_{i\perp}^2}\Big)_{\text{eq}}$$

Table 3. Parameters of the rigid ion model in $LiYF_4$ after the fitting procedure used in this paper. The short-range force constants reported in italic have been calculated from the F–F interionic potential given in [4] and were kept constant during the fitting procedure. For an easier comparison, we also report the most important short-range force constants that have been deduced by other authors in compounds which involve the same ionic pairs: Dörfler [10] for $LiTbF_4$, Boumriche *et al* [16] in $BaLiF_3$, and those we deduced from the Li-F interionic potentials from Catlow *et al* [17] with the appropriate distance.

	i	Ion pair	d_i (Å)	A_i (N m^{-1})	B_i (N m^{-1})
For this paper [a]	1	Li–F	1.898	64.0	−10.0
$LiYF_4$	2	Y–F	2.244	134.4	−11.2
	3	Y-F	2.297	116.7	−10.3
	4	F–F	2.597	18.0	−3.2
	5	F–F	2.747	*12.7*	*−2.7*
	6	F–F	2.767	*12.2*	*−2.6*
	7	F–F	2.832	*11.1*	*−2.3*
	8	Li–F	2.898	5.4	−0.9
	9	F–F	2.954	*8.9*	*−1.7*
For other authors [b]		Li–F	1.897	71.1	−12.4
$LiTbF_4$ [13]		Y–F	2.272	133.3	−13.5
		Y–F	2.321	119.9	−10.8
$BaLiF_3$ [15]		Li–F	1.998	46.2	−1.717
LiF [16]		Li–F	1.898	set 1 80.3	−11.1
(interionic potentials)				set 2 86.8	−12.6

Ionic effective charges (expressed in $|e|$ units).
[a] $Z_F^* = -0.770$ (imposed); $Z_{Li}* = 0.757$ ($Z_Y* = 2.323$).
[b] $LiTbF_4$: $Z_F^* = -0.785$; $Z_{Li}^* = 0.889$ ($Z_{Tb}^* = 2.250$);
$BaLiF_3$: $Z_F^* = -0.771$; $Z_{Li}^* = 0.759$ ($Z_{Ba}^* = 1.554$);
LiF: set 1 $Z_F^* = -0.981$, set 2 effective charges.

where eq stands for equilibrium position and i refers to the ith pair of ions. As previously carried out by Dörfler [10] for the isomorphic compound $LiTbF_4$, we will consider the nine shortest distances, which yield 18 short-range parameters in the model.

The electrostatic long-range interactions will be defined through effective ionic charges Z_i^* [11]. Due to the condition of charge neutrality, this gives two further parameters. Thus, even in this simple model, a total of 20 parameters has to be considered.

To decrease the number of adjustable parameters, we used the information from [4] to fix the effective charge to $-0.77|e|$ and to calculate the fluorine–fluorine (F–F) short-range force constants (SRFCs) from the Born–Mayer potential:

$$V_{F-F}(r) = \lambda \exp(-r/\rho) \qquad \text{with } \rho = 0.582 \text{ Å and } \lambda = 481 \text{ Nm}^{-1}\text{Å}^{-2}$$

The only exception concerns the shortest F–F distance (see table 3) which is well under the distances for which the Born–Mayer parameters have been calculated (2.8–3.2 Å); the corresponding short-range parameters A_4 and B_4 hence remained free during the fitting procedure.

The remaining 11 parameters in the model have been adjusted with the help of the *GENAX2* program of Reichardt, implemented at the LLB. The starting model was based on the zone-centre phonons [12–14], infrared or Raman active (see paper I), and on the slopes of acoustic branches in the three main directions ΓKZ, $Z\Gamma$ and ΓX of the reciprocal lattice, as deduced from ultrasonic velocities measurements [15]. Then, the successive models were improved by including the latest inelastic neutron-scattering results, taking into account both the frequencies of the modes and the corresponding intensities. Such an

Table 4. Frequencies (in THz) of zone-centre phonons in $LiYF_4$ at room temperature. Calc index: frequencies calculated with the parameters of the rigid ion model presented in table 3. Meas index: measured frequencies (see paper I). The average discrepancy between the 29 measured zone-centre phonons and their calculated value is 4.6%.

Raman active modes: $\overline{\Delta\nu/\nu} = 3.5\%$

A_g			B_g			E_g		
ν_{meas} (THz)	ν_{calc} (THz)	$\Delta\nu/\nu$ (%)	ν_{meas} (THz)	ν_{calc} (THz)	$\Delta\nu/\nu$ (%)	ν_{meas} (THz)	ν_{calc} (THz)	$\Delta\nu/\nu$ (%)
4.53	*4.47*	**1.3**	5.22	*5.64*	**8**	4.62	*4.56*	**1.3**
7.95	*7.17*	**9.8**	7.38	*7.75*	**5**	5.97	*6.35*	**6.3**
12.81	*12.58*	**1.8**	9.81	*9.57*	**2.4**	9.78	*9.35*	**4.4**
			11.37	*11.08*	**2.5**	11.19	*11.35*	**1.4**
			12.81	*12.68*	**1**	13.41	*13.45*	**0.3**
	$\overline{\Delta\nu/\nu}$	**4.3**%			**3.8**%			**2.7**%

Infrared active modes: $\overline{\Delta\nu/\nu} = 5.5\%$ (5.7% for TO modes and 5.35% for LO modes).

	A_u				E_u		
	ν_{meas} (THz)	ν_{calc} (THz)	$\Delta\nu/\nu$ (%)		ν_{meas} (THz)	ν_{calc} (THz)	$\Delta\nu/\nu$ (%)
TO1	5.94	*5.75*	**3.2**	TO1	4.11	*4.69*	**14.1**
LO1	6.6	*6.15*	**6.8**	LO1	5.13	*5.86*	**14.2**
TO2	7.53	*8.17*	**8.5**	TO2	8.83	*8.38*	**5**
LO2	8.41	*8.94*	**6.3**	LO2	9.24	*8.78*	**5**
TO3	10.19	*9.71*	**4.7**	TO3	9.75	*9.67*	**0.8**
LO3	10.84	*11.61*	**7.1**	LO3	11.01	*10.81*	**1.8**
TO4	11.16	*12.08*	**8.2**	TO4	12.54	*12.72*	**1.4**
LO4	16.11	*15.91*	**1.2**	LO4	16.8	*16.87*	**0.4**
		$\overline{\Delta\nu/\nu}$	**TO: 6.15**				**TO: 5.3**
			LO: 5.35				**LO: 5.35**

approach was necessary due to the small number of different symmetries (see section 2) and to the large number of dispersion branches in a fairly narrow frequency range (the cut-off frequency in fluoride compounds is generally below 600 cm^{-1}).

The final set of parameters has been reported in the first part of table 3. With these values, the average discrepancy between calculated and measured frequencies was less than 5%, even for zone-centre modes, as shown in table 4.

As seen in the first part of table 3, the Y–F interactions yield the strongest SRFCs, even though the corresponding interionic distances are much greater than the shortest Li–F one. This is obviously due to the difference of valence between interacting ions, namely +III/−I for a Y–F pair, and only +I/ − I for a Li–F pair. No short-range force constants for Y–F interactions are reported in the literature, but the values we obtained can be compared with the Tb–F SRFCs in $LiTbF_4$ [10] (see the second part of table 3). Y^{3+} and Tb^{3+} have indeed the same external electronic configuration ($5s^o$ and $6s^o$ respectively), and their ionic radii, within a coordinate of eight fluorine ions, are very close (1.16 and 1.18 Å respectively [1]). Concerning Li–F interactions, our values may be directly compared (see table 3) to those obtained in $LiTbF_4$ [10], $BaLiF_3$ [4, 16], and to the values we may deduce, with the adapted distance, from Li–F interionic potentials [17] defined in LiF, a NaCl-type crystal. Finally, the two parameters A_4 and B_4 which remained free during the fitting procedure only deviate by 10% from their initial value, deduced from the F–F interionic potential. The values

obtained for these particular two parameters are also consistent with those obtained in MF_3 compounds (M = Al, Ga, Cr, Fe, V) where the same interionic distances are encountered [18].

4.2. Calculated phonon dispersion curves, density of states and atomic movements

4.2.1. Phonon dispersion curves. The dispersion curves, calculated with the model described above, are drawn in figure 4 together with experimental data along the [100], [110] and [001] directions of the quadratic Brillouin zone. For clarity, the frequency interval has been limited to [0, 8THz]. The agreement between calculated and measured dispersion curves is generally fairly good, even though some systematic discrepancies may be pointed out. The first one comes from the fact that we did not succeed in avoiding the permutation of the first E_u (TO) and E_g modes between model and experiment. The other one concerns the two lowest-frequency modes at the X point. Indeed they are depending on several orthoradial force constants (B_i) which are also involved in modes at X, Z and Γ points. The reported RIM parameters are those that lead to the best compromise.

Nonetheless, it is worth noting that we have obtained an overall agreement on 29 Raman and IR frequencies and our neutron data, including dynamical structure factors, with the refinement of only 11 parameters. This supports the assumption that we have made of the transferability of the F–F interionic potential.

4.2.2. One-phonon density of states. The one-phonon density of states $g(\omega)$ has been calculated using the set of parameters from the first part of table 3. The result is plotted in figure 5(a). The calculated cut-off frequency is in the vicinity of 600 cm^{-1}, as generally observed in fluoride compounds.

Figure 5(b) shows the partial density of states $g_i(\omega)$, with $g(\omega) = g_{Li}(\omega) + g_Y(\omega) + g_F(\omega)$, which represent the weighted contribution of each ionic species. Three frequency intervals may be considered:

(1) 0–$\sim$200 cm^{-1}: $g_F(\omega)$ and $g_Y(\omega)$ are quite identical, whereas $g_{Li}(\omega)$ is near zero; the vibrations in this frequency range essentially imply ions of the YF_8 'double tetrahedron'.

(2) 400–$\sim$600 cm^{-1}: here, $g_F(\omega)$ and $g_{Li}(\omega)$ are quite identical, while $g_Y(\omega)$ is near zero; the vibrations essentially imply motions in or between LiF_4 tetrahedra.

(3) 200–$\sim$400 cm^{-1}: in this intermediate frequency range, $g_{Li}(\omega)$ and $g_Y(\omega)$ are quite weak compared with $g_F(\omega)$; hence the vibrations are essentially those of fluorine ions.

Nonetheless, there are no real gaps between these three 'categories' of modes as could occur in oxide scheelites where one can discriminate between internal and external modes. In the present case, only lattice dynamical calculations may bring information on the real atomic movements.

4.2.3. Calculated atomic displacements. We reported in figure 6 the main components of the calculated eigenvectors corresponding to some of the Raman or IR-active modes. These movements may be expressed on the basis of the 'modes' that have been defined by Miller *et al* [13] in terms of internal coordinates compatible with the symmetry. It can be seen, for example, that the third A_g mode (12.81 THz) is associated with a stretching of the LiF_4 tetrahedron; the second B_g mode may be described as an angular deformation of the LiF_4 entity and so on. Nonetheless, the movements are generally much more complicated, but they can always be decomposed in a sum of Miller's 'modes': the first transversal E_u mode (ν(TO1) = 4.11 THz) is then a combination of a Y^{3+} translation in the (001) plane, plus a rotation around the a-axis of the fluorine ions in LiF_4, and finally an angular distortion

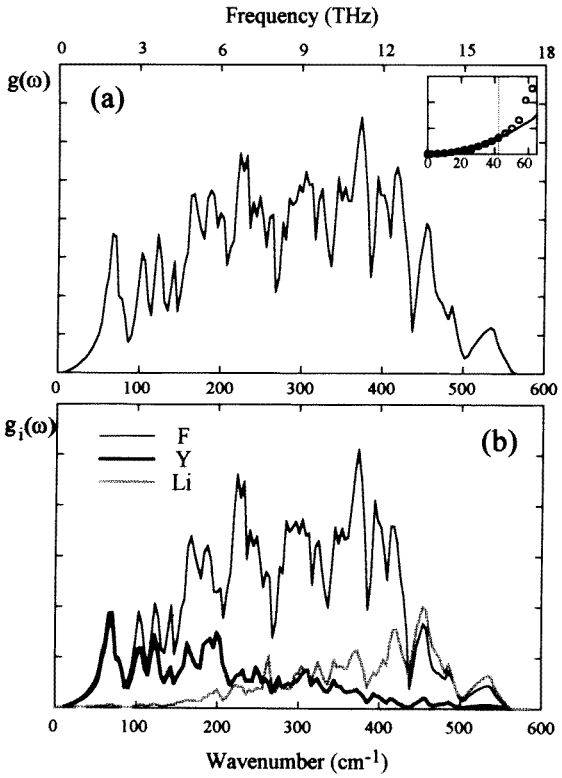

Figure 5. The normalized one-phonon density of states calculated within a rigid ion model with an energy step of 0.5 meV: (*a*) $g(\omega)$, total density of states. Inset: detail of the low-frequency range, the full curve represents the behaviour according to Debye's law $g(\omega)\alpha\omega^2$. (*b*) $g_i(\omega)$, partial density of states for each kind of atom with $g_{\mathrm{Li}}(\omega) + g_{\mathrm{Y}}(\omega) + g_{\mathrm{F}}(\omega) = g(\omega)$.

('ν_2'). So the present modelization shows that most of the Raman and infrared active modes of $LiYF_4$ cannot be described in terms of simple vibrations of the polyhedra. This is a consequence of the strong coupling between internal and external modes as previously mentioned about the density of states.

In paper I, the comparison of the frequencies of zone-centre vibrational modes in the Li*Ln*F_4 series of compounds (*Ln* = Ho, Er, Tm, Yb; Y) has shown that, surprisingly, the heavy *Ln* ions are not involved in the lowest frequency A_u and E_u modes, their frequencies being not dependent on the trivalent ion's nature. The present model is in agreement with such a behaviour, the Y atoms being at rest for these two modes. On the other hand, our calculations show that the two lowest frequency B_g and E_g modes and the two following A_u and E_u modes imply important movements of Y^{3+}, as experimentally observed: these modes are the most significantly affected by the substitution of heavier *Ln* for Y.

5. Conclusion

This work gives a description of the lattice dynamics in scheelite compounds, including the irreducible representations of the wavevectors point groups, the corresponding symmetry-adapted eigenvectors and their compatibility relations at high symmetry points of the

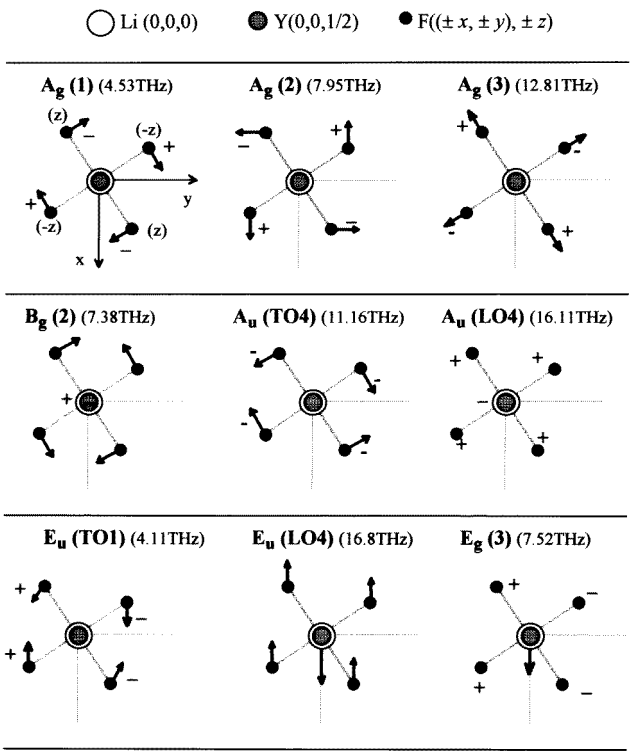

Figure 6. Main components of the eigenvectors corresponding to some of the Raman- and infrared-active modes, calculated with the rigid ion model presented in table 3 (with experimental frequencies in parentheses). The displacements are only represented for half the unit of structure, the displacements of the other ions in the primitive- cell being deduced by the inversion symmetry operation (see figure 1), with respect to the symmetry of the mode under consideration, namely u (antisymmetric) or g (symmetric).

Brillouin zone. The dispersion curves and the phonon density of states have been determined for the fluoride scheelite $LiYF_4$. The experimental study by inelastic neutron scattering as well as the calculations show that, in opposition to oxide scheelites where internal and external modes can be differentiated, these are coupled in fluoride scheelites.

The parameters of a rigid ion model have been deduced by using a F–F interionic potential, previously determined in fluoride perovskites, to impose the F–F parameters, and adjusting the other force constants. The proposed model reproduces satisfactorily the experimental frequencies, measured either by inelastic neutron-scattering or by IR and Raman scattering; it also gives a reliable description of the peak intensities in the inelastic neutron-scattering spectra. Hence this model seems to be well adapted to calculate the vibronic contribution in the luminescence spectra of $LiYF_4$ doped with ions like U^{3+} and Ce^{3+} for which the electron–phonon coupling is stronger than usually observed for rare-earth ions.

As already mentioned, we obtained a correct description of the $LiYF_4$ experimental phonon spectra even though half of the parameters in the rigid ion model have been imposed on the basis of a F–F interionic potential determined in compounds with a different structure. This is a good indication that this potential may be transposed from one crystalline

structure to another. Thus phonon spectra calculated with the same method in more complex structures than scheelites should be reliable. Such a calculation in β–YF_3 is in progress. Besides, the Y–F and Li–F short-range force constants we have obtained may now be used to the determination of corresponding interionic potentials.

Acknowledgment

We are extremely grateful to Dr W Reichardt for having made us aware of such a user-friendly program for lattice dynamical calculations and, above all, for his helpful comments about the results obtained in this study.

References

[1] Kaminskii A 1990 *Laser Crystals* (Berlin: Springer)
[2] Meichenin D, Auzel F, Hubert S, Simoni E, Louis M and Gesland J Y 1994 *Elec. Lett.* **30** 1309
[3] Bulou A, Rousseau M and Nouet J 1992 *Key Engineering Materials* vol 68 (Switzerland: Trans. Tech Publications) pp 133–86
[4] Salaün S and Rousseau M 1995 *Phys. Rev.* B **51** 15 867
[5] Maradudin A A and Vosko S H 1968 *Rev. Mod. Phys.* **40** 1
[6] Zak J, Cacher A, Gluck H and Gur Y 1969 *The Irreducible Representations of Space Groups* (New York: Benjamin)
[7] Garcia E and Ryan R R 1993 *Acta Crystallogr.* C **49** 2053
[8] Born M and Huang K 1954 *Dynamical Theory of Crystal Lattices* (London: Oxford University Press)
[9] Cowley R A 1964 *Phys. Rev.* **134** 981
[10] Dörfler W 1984 *PhD Thesis* University of Würtzburg, Germany
[11] Szigeti B 1950 *Proc. R. Soc.* A **204** 51
[12] Fornoni M T 1991 *PhD Thesis* Université du Maine, Le Mans, France
[13] Miller S A, Rast H E and Caspers H H 1970 *J. Chem. Phys.* **52** 4172
[14] Schulteiss E, Scharmann A and Schwabe D 1986 *Phys. Status Solidi* **138** 465
[15] Blanchfield P and Saunders G A 1979 *J. Phys. C: Solid State Phys.* **12** 4673
[16] Boumriche A, Gesland J Y, Bulou A, Rousseau M, Fourquet J L and Hennion B 1994 *Solid State Commun.* **91** 125
[17] Catlow C R A, Diller K M and Norgett M J 1977 *J. Phys. C: Solid State Phys.* **10** 1395
[18] Daniel P, Bulou A, Rousseau M, Nouet J and Leblanc M *Phys. Rev.* B **42** 10 545